Research Square

Preprints are preliminary reports that have not undergone peer review.
They should not be considered conclusive, used to inform clinical practice,
or referenced by the media as validated information.

Compositionally tuned electrospun spinel nanofibers: phase-specific redox chemistry and battery-type charge storage in $CoFe_2O_4$, $CuCo_2O_4$ and $CuNi_2O_4$

Pengyu Mao
Chengdu University of Technology
Hengquan Liu
liuhengquan15@cdut.edu.cn
Chengdu University of Technology
Yujie Liu
Chengdu University of Technology
Mengyang Li
Chengdu University of Technology

Research Article

Keywords: electrospinning, spinel oxide nanofibers, composition regulation, battery-type electrode, charge-storage kinetics, asymmetric supercapacitor

Posted Date: November 24th, 2026

DOI: https://doi.org/10.21203/rs.3.rs-11755561/v1

License: This work is licensed under a Creative Commons Attribution 4.0 International License.
Read Full License

Additional Declarations: No competing interests reported.

Compositionally tuned electrospun spinel nanofibers: phase-specific redox chemistry and battery-type charge storage in $CoFe_2O_4$, $CuCo_2O_4$ and $CuNi_2O_4$

Pengyu Mao[1], Hengquan Liu[1,2]*, Yujie Liu[1], Mengyang Li[1]

[1]*College of Materials and Chemistry & Chemical Engineering, Chengdu University of Technology, Chengdu 610059, China*

[2]*College of Materials and Energy, Guang'an Institute of Technology, Guang'an 638550, China*

*Corresponding author: Hengquan Liu

Email:liuhengquan15@cdut.edu.cn

Abstract

Electrospun spinel oxides are attractive battery-type electrode materials, but comparisons among compositions are often confounded by changes in precursor chemistry, morphology and thermal treatment. Here, $CoFe_2O_4$, $CuCo_2O_4$ and $CuNi_2O_4$ nanofibers were prepared under identical PVP/DMF electrospinning, pre-oxidation and calcination conditions. Phase-specific X-ray diffraction peak groups were indexed separately against the corresponding reference cards rather than forced onto a common set of reflections. X-ray photoelectron spectroscopy identified Co^{2+}/Co^{3+} and Fe^{3+} in $CoFe_2O_4$, Cu^{2+} and Co^{2+}/Co^{3+} in $CuCo_2O_4$, and Cu^{2+} and Ni^{2+}/Ni^{3+} in $CuNi_2O_4$, together with lattice and surface oxygen species. In 1 mol L^{-1} KOH, the electrodes delivered specific capacitances of 484, 406 and 220 F g^{-1} at 1 A g^{-1} for $CuCo_2O_4$, $CoFe_2O_4$ and $CuNi_2O_4$, respectively. $CoFe_2O_4$ exhibited the best relative rate retention, reaching approximately 54% at 4 A g^{-1}, compared with approximately 49% for $CuNi_2O_4$ and 41% for $CuCo_2O_4$. Cyclic-voltammetry analysis showed battery-like Faradaic behavior with composition-dependent surface and diffusion contributions. A $CuCo_2O_4$//activated-carbon device retained 99.93% of its initial capacitance and a coulombic efficiency of 99.96% after 5000 cycles. The comparison shows that cation composition controls the balance among accessible redox centers, charge-transfer resistance and ion transport more strongly than fiber diameter alone.

Keywords: electrospinning; spinel oxide nanofibers; composition regulation; battery-type electrode; charge-storage kinetics; asymmetric supercapacitor

1 Introduction

Electrochemical capacitors bridge the performance gap between dielectric capacitors and batteries, but their practical energy density remains limited by the electrode material and cell design [1, 2]. Carbon-based electrodes provide high power and long cycle life through electric double-layer storage, although their moderate charge-storage capacity restricts the achievable energy density [3, 4]. Transition-metal oxides can store charge through reversible Faradaic reactions and therefore offer higher capacity, but poor electronic conductivity, limited ion transport and structural degradation continue to compromise rate performance and durability [5, 6]. These limitations are particularly important when oxide powders require insulating binders and conductive additives that add inactive mass and obstruct active sites [7-9].

Electrospinning offers a direct route to continuous oxide nanofiber networks with high aspect ratio, interconnected porosity and short transport distances [10-14]. The morphology is controlled by solution rheology, electric-field conditions and thermal conversion, while the final phase and surface chemistry depend on metal stoichiometry, cation distribution and calcination history [15-18]. Consequently, morphology and composition effects are difficult to separate when samples are prepared under different conditions. A comparison that fixes the processing protocol is needed to determine whether the electrochemical differences originate from phase chemistry, surface valence, transport resistance or geometric accessibility [19-22].

Spinel oxides are especially relevant because their tetrahedral and octahedral cation sites can accommodate multiple transition metals and oxidation states [4, 18]. $CoFe_2O_4$ generally combines iron and cobalt redox centers, $CuCo_2O_4$ offers coupled Cu/Co redox chemistry, and $CuNi_2O_4$ contains Cu and Ni centers with different hydroxide affinities and electronic structures. Recent studies in Ionics have examined Sr-doped $CuCo_2O_4$ [36], ternary $CuNiMnO_4$/MWCNT composites [37] and composition-tailored $CuNi_2O_4$ [38], demonstrating strong interest in spinel electrodes for hybrid charge storage. Carbon-containing composites and single-composition optimization, however, introduce additional interfacial or processing variables. A controlled three-spinel comparison under the same electrospinning and calcination conditions is therefore useful for identifying composition-dependent structure–property relationships.

In this work, $CoFe_2O_4$, $CuCo_2O_4$ and $CuNi_2O_4$ nanofibers were synthesized using the same PVP/DMF precursor route and thermal schedule. Phase-specific XRD assignments, surface-valence analysis by XPS, matched-window cyclic voltammetry, impedance spectroscopy and galvanostatic measurements were combined to answer three questions: which spinel provides the highest accessible capacity, which composition supports the best rate

retention, and how charge-transfer and diffusion limitations differ among the three fiber networks. The study does not claim that one spinel is universally superior; instead, it resolves composition-dependent trade-offs that are relevant to the rational selection of spinel supercapacitor electrodes.

2 Experimental

2.1 Materials and synthesis

N,N-dimethylformamide (DMF), N-methyl-2-pyrrolidone (NMP), $Ni(NO_3)_2·6H_2O$, $Co(NO_3)_2·6H_2O$, $Fe(NO_3)_3·9H_2O$, $Cu(NO_3)_2$, polyvinylpyrrolidone (PVP), acetylene black and polyvinylidene fluoride (PVDF) were of analytical grade and used as received. Nickel foam was cut into 1 × 1 cm² pieces, ultrasonically cleaned in 1 mol L^{-1} HCl for 5 min, rinsed with acetone, ethanol and deionized water, and dried before use.

Three precursor solutions were prepared with fixed total metal nitrate stoichiometry. For $CoFe_2O_4$, 1 mmol $Co(NO_3)_2·6H_2O$ and 2 mmol $Fe(NO_3)_3·9H_2O$ were dissolved in 10 mL DMF. For $CuCo_2O_4$, 1 mmol $Cu(NO_3)_2$ and 2 mmol $Co(NO_3)_2·6H_2O$ were used. For $CuNi_2O_4$, 1 mmol $Cu(NO_3)_2$ and 2 mmol $Ni(NO_3)_2·6H_2O$ were used. Then, 1.8 g PVP was added to each solution, and the mixtures were stirred for 10–12 h. Electrospinning was performed at 12 kV with a tip-to-collector distance of 12 cm. The as-spun mats were dried at 60 °C for 12 h and heated at 1 °C min^{-1} to 250 °C for 2 h and then to 500 °C for 2 h in air.

Working electrodes were prepared by mixing the active fibers, PVDF and acetylene black at a mass ratio of 8:1:1 in NMP. The slurry was coated onto pretreated nickel foam and dried at 60 °C for 12 h. The same electrode-preparation procedure was used for all three oxides.

2.2 Materials characterization

XRD patterns were recorded on a DX-2700BH diffractometer (Dandong, China) over 5–80° 2θ at 8° min^{-1}. The observed peak groups were compared with the phase cards $CoFe_2O_4$ PDF 79-1744, $CuCo_2O_4$ PDF 25-0270 and $CuNi_2O_4$ PDF 78-0648. Reported positions were read from the plotted patterns to approximately ±0.2° and are used for phase identification, not for Rietveld refinement.

Morphology and elemental distribution were examined using field-emission scanning electron microscopy (ZEISS Gemini 360) equipped with an UltimMax40 energy-dispersive X-ray spectrometer. XPS was performed on a Thermo Fisher K-Alpha instrument using monochromatic Al Kα radiation at 12 kV. Binding energies were calibrated to the C 1s peak at 284.8 eV. Principal component and satellite positions were read from the fitted spectra. Because the original fitted component areas were not available, no quantitative Co^{2+}/Co^{3+} or Ni^{2+}/Ni^{3+} ratios were calculated.

2.3 Electrochemical measurements and calculations

Electrochemical measurements were performed on a CS2350M workstation (Corrtest, Wuhan, China) in 1 mol L^{-1} KOH using a three-electrode configuration, with the fiber electrode, platinum foil and Hg/HgO as working, counter and reference electrodes, respectively. Cyclic voltammetry (CV), galvanostatic charge–discharge (GCD) and electrochemical impedance spectroscopy (EIS) were recorded. The matched-window CV comparison used 0.1–0.6 V versus Hg/HgO. Individual scan-rate series were measured in the potential windows shown in the figure and are not compared solely by enclosed area.

Specific capacitance was calculated from GCD curves according to $Cs = I\Delta t/(m\Delta V)$, where I is the discharge current (A), Δt is the discharge time (s), m is the active mass (g) and ΔV is the potential window corrected for IR drop (V). Coulombic efficiency was calculated as $CE = (td/tc) \times 100\%$, where td and tc are the discharge and charge times. Surface- and diffusion-controlled current fractions were evaluated using $i(v) = k_1v + k_2v^{1/2}$. The resulting fractions are treated as empirical fitting descriptors rather than as a universal mechanistic classification.

Asymmetric devices were assembled in CR2032 coin cells using $CuCo_2O_4$ as the positive electrode, activated carbon as the negative electrode, 6 mol L^{-1} KOH as the electrolyte and glass-fiber filter paper as the separator. Cycling and GCD stability were evaluated on a LAND battery-testing system.

3 Results and discussion

3.1 Phase structure and XRD indexing

The XRD patterns in Fig. 1 contain three distinct phase-specific reflection families. The reflection groups are summarized in Table 1 and should not be treated as a common set of spinel peaks at 30°, 35°, 37°, 43°, 57° and 62°. The $CoFe_2O_4$ trace is broad and contains weak features near 30.2°, 35.6°, 43.2°, 57.2° and 62.8°. $CuCo_2O_4$ shows a more split pattern, including features near 31.4°, 36.8°, 44.0°, 55.0°, 59.0° and 65.0°, together with a low-angle feature near 19°. $CuNi_2O_4$ displays strong peaks near 36.5°, 38.0°, 42.6°, 62.0° and 74.4°, with an additional weak feature near 31.8°. These differences are consistent with the three different reference cards and with changes in lattice parameter and cation distribution.

The broad $CoFe_2O_4$ peaks indicate small coherent domains, structural disorder or strain and do not by themselves indicate an impure phase. Likewise, the sharper $CuNi_2O_4$ pattern cannot be attributed solely to its larger fiber diameter, because nucleation and crystallite growth during calcination depend on cation chemistry, phase stability and oxygen loss as well as on local precursor confinement. The XRD data therefore establish phase identity and relative crystallinity trends, but they do not support a direct one-to-one causal relation between fiber diameter and crystallinity.

Table 1 Approximate XRD peak groups observed for the three electrospun spinel fibers. Positions were read from the plotted patterns (±0.2°) and are provided for phase identification only

Sample	Observed 2θ groups (°)	Reference card	Structural interpretation
$CoFe_2O_4$	30.2, 35.6, 43.2, 57.2, 62.8	PDF 79-1744	Broad spinel reflections; nanoscale domains and/or structural disorder
$CuCo_2O_4$	19.0, 31.4, 36.8, 44.0, 55.0, 59.0, 65.0	PDF 25-0270	Split, phase-specific reflection groups; no precursor peaks detected
$CuNi_2O_4$	31.8, 36.5, 38.0, 42.6, 62.0, 74.4	PDF 78-0648	Sharper spinel reflections shifted from the Co-containing phases

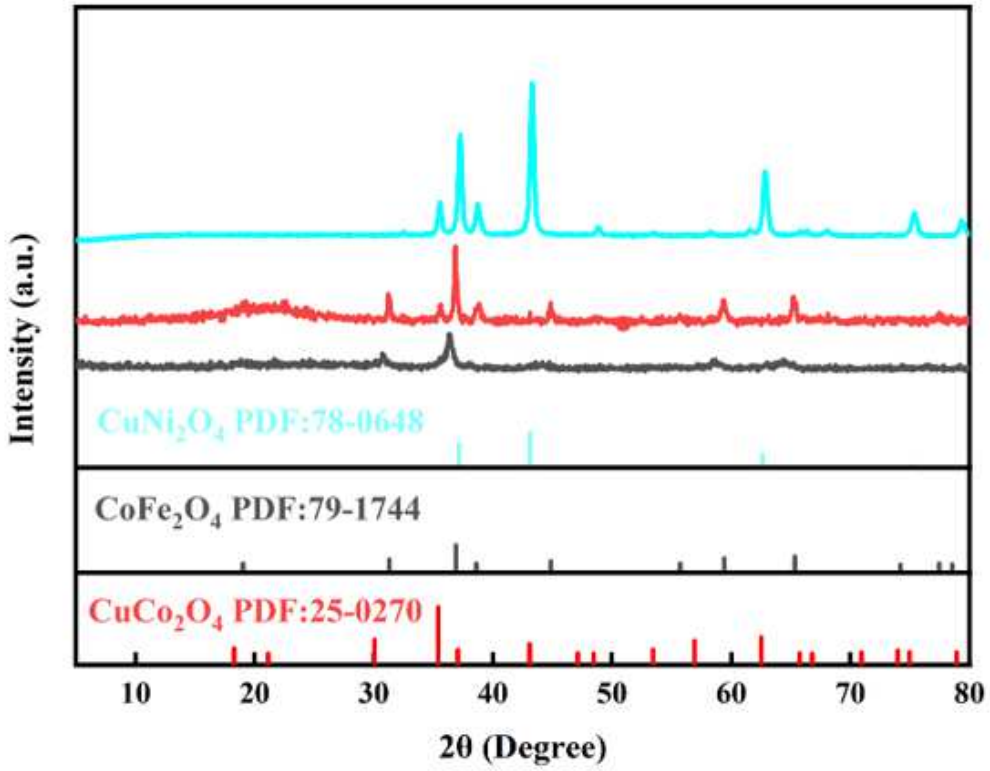


Fig. 1 XRD patterns of electrospun $CoFe_2O_4$, $CuCo_2O_4$ and $CuNi_2O_4$ nanofibers together with the corresponding reference cards. The three phases are indexed as separate reflection families; peak positions are summarized in Table 1

3.2 Morphology and elemental distribution

SEM images in Fig. 2 show continuous, interconnected fibers with rough surfaces composed of fine oxide grains. The average diameters of $CoFe_2O_4$, $CuCo_2O_4$ and $CuNi_2O_4$ are approximately 129, 146 and 172 nm, respectively. The persistence of the one-dimensional network after calcination indicates that the entangled PVP chains confined the metal precursors and limited macroscopic aggregation. EDS maps show uniform metal and oxygen distributions for each sample, consistent with homogeneous precursor mixing before pyrolysis.

Fiber diameter affects electrolyte accessibility, but it is not sufficient to explain the electrochemical ordering. $CuNi_2O_4$ has the largest average diameter yet the smallest high-frequency EIS semicircle, whereas $CuCo_2O_4$ has

the highest low-current capacitance despite an intermediate diameter. These observations point to a combined influence of surface valence, electronic conduction and ion transport, which is examined below.

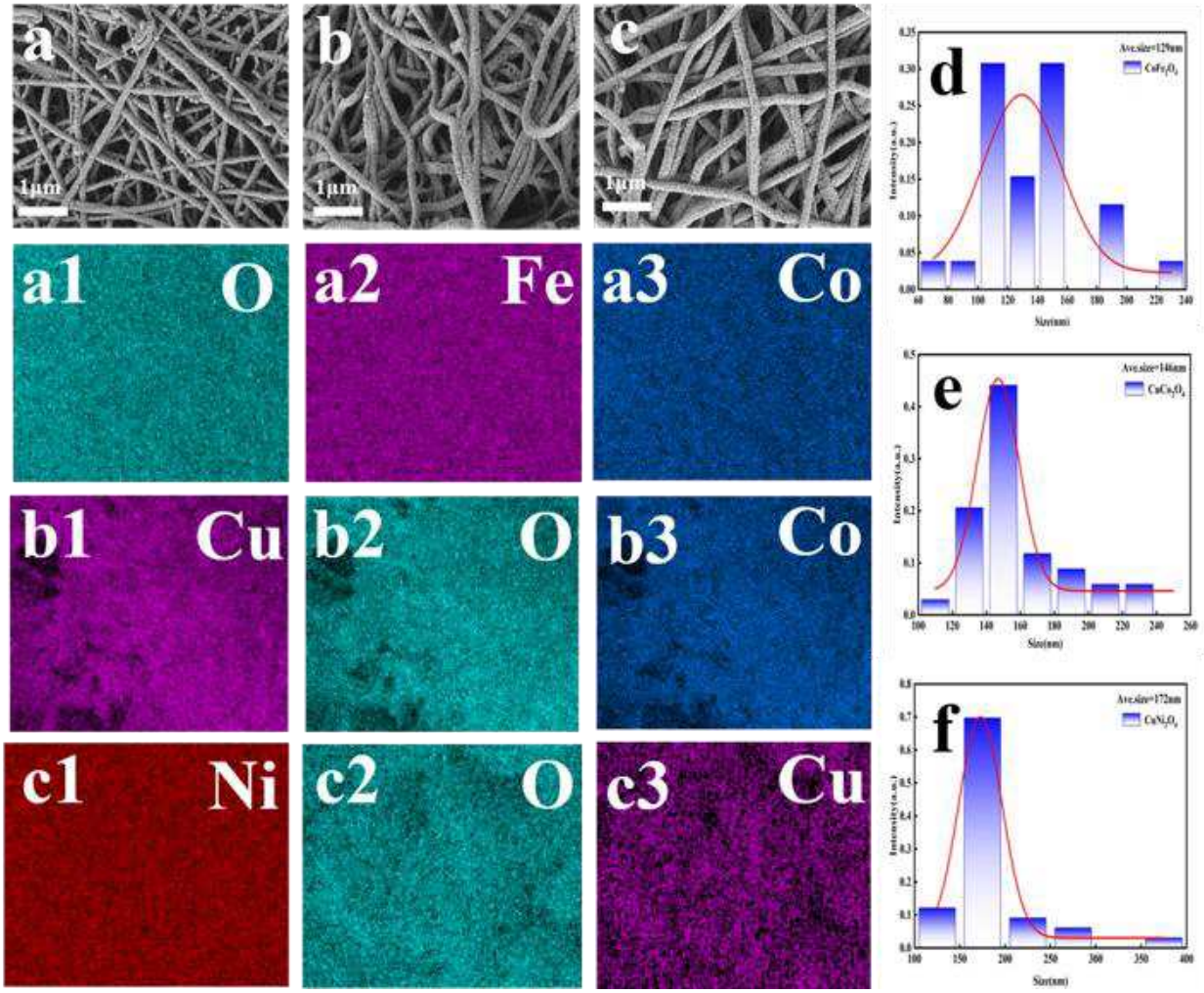


Fig. 2 SEM images, EDS maps and fiber-diameter distributions of (a) $CoFe_2O_4$, (b) $CuCo_2O_4$ and (c) $CuNi_2O_4$; (d–f) corresponding diameter distributions

3.3 Surface composition and valence states

The high-resolution XPS panels in Fig. 3 are presented at enlarged scale, and the principal binding energies are listed separately in Table 2. All spectra were charge-corrected to C 1s at 284.8 eV. For $CoFe_2O_4$, the Co $2p_{3/2}$ and Co $2p_{1/2}$ components near 779.5 and 794.7 eV, together with their satellite structures, indicate mixed Co^{2+}/Co^{3+} character. The Fe $2p_{3/2}$ component near 710.6 eV and the Fe $2p_{1/2}$ component near 724.1 eV are consistent with Fe^{3+}. For $CuCo_2O_4$, Cu $2p_{3/2}$ and Cu $2p_{1/2}$ features near 933.4 and 953.2 eV indicate Cu^{2+}, while Co 2p components near 779.7 and 795.0 eV again indicate mixed Co valence. In $CuNi_2O_4$, Ni $2p_{3/2}$ and Ni $2p_{1/2}$ features near 855.7 and 873.4 eV, together with the Cu 2p features near 933.6 and 953.6 eV, support the coexistence of Ni^{2+}/Ni^{3+} and Cu^{2+}.

The O 1s spectra contain a dominant lattice-oxygen component near 529 eV and higher-binding-energy components associated with surface hydroxyl groups, defect-related oxygen and adsorbed oxygen. These surface species can influence hydroxide adsorption and interfacial charge transfer, but their populations are not quantified here. The XPS data therefore establish the available redox centers and surface oxygen chemistry rather than a quantitative site distribution. This distinction is important because fitted-area ratios derived from a single, overlapping 2p envelope are sensitive to background and line-shape constraints [23, 24].

Table 2 Principal XPS binding energies of the electrospun spinel fibers. Values are approximate component positions read from the fitted spectra and are rounded to 0.1 eV

Sample	Region	Principal components (eV)	Satellite / shoulder features (eV)	Assignment
$CoFe_2O_4$	Co 2p	779.5, 794.7	≈786, ≈802	Co^{2+}/Co^{3+} multiplet structure
$CoFe_2O_4$	Fe 2p	710.6, 724.1	≈718, ≈732	Fe^{3+} with shake-up satellites
$CoFe_2O_4$	O 1s	529.0	≈530.8, ≈532.2	Lattice O; OH/Ovac/adsorbed O
$CuCo_2O_4$	Cu 2p	933.4, 953.2	≈941–943, ≈961–963	Cu^{2+} and shake-up satellites
$CuCo_2O_4$	Co 2p	779.7, 795.0	≈786, ≈802	Co^{2+}/Co^{3+} multiplet structure
$CuCo_2O_4$	O 1s	529.1	≈530.8, ≈532.1	Lattice O; surface oxygen species
$CuNi_2O_4$	Ni 2p	855.7, 873.4	≈861, ≈879	Ni^{2+}/Ni^{3+} multiplet structure
$CuNi_2O_4$	Cu 2p	933.6, 953.6	≈941–943, ≈961–963	Cu^{2+} and shake-up satellites
$CuNi_2O_4$	O 1s	529.0	≈530.8, ≈532.2	Lattice O; OH/Ovac/adsorbed O

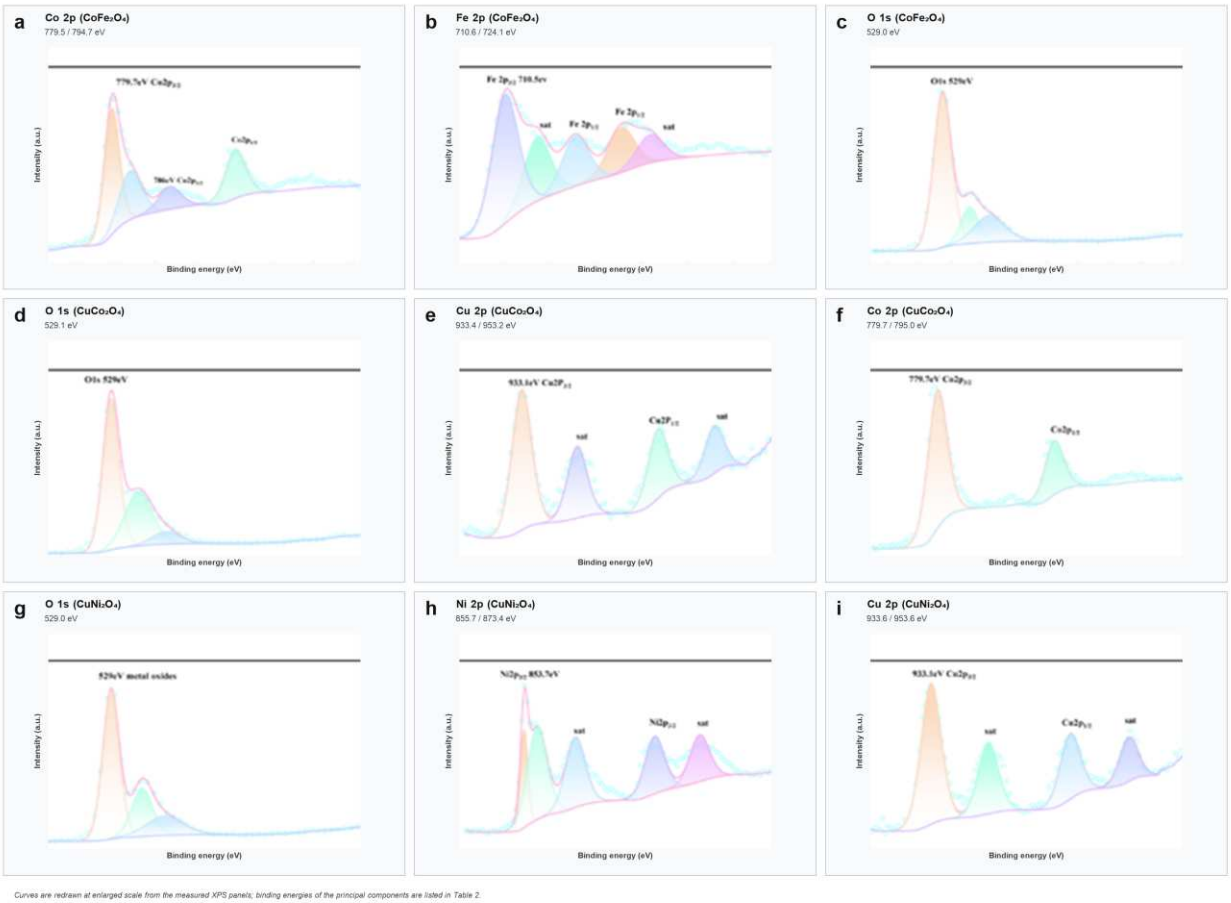


Fig. 3 XPS spectra of the three spinel nanofibers: (a) Co 2p, (b) Fe 2p and (c) O 1s for $CoFe_2O_4$; (d) O 1s, (e) Cu 2p and (f) Co 2p for $CuCo_2O_4$; and (g) O 1s, (h) Ni 2p and (i) Cu 2p for $CuNi_2O_4$. Principal binding energies are given above each panel and in Table 2

3.4 Charge-transfer and redox kinetics

The Nyquist plots in Fig. 4 show small real-axis intercepts for all electrodes, indicating comparable series resistance and contact resistance. The high-frequency semicircle is smallest for $CuNi_2O_4$, followed by $CuCo_2O_4$ and $CoFe_2O_4$. This ordering indicates faster interfacial charge transfer for $CuNi_2O_4$ under the measured conditions. The low-frequency slope, however, is less steep for $CuNi_2O_4$, which indicates greater restriction to long-range ion diffusion or a less ideal porous response. A small charge-transfer semicircle and a steep diffusion tail therefore describe different processes and need not produce the same capacitance ranking [25, 26].

Panel 5a compares the three electrodes at 5 mV s^{-1} in the same 0.1–0.6 V window. $CuCo_2O_4$ and $CoFe_2O_4$ exhibit larger redox currents and integrated areas than $CuNi_2O_4$, while all three show asymmetric oxidation and reduction features rather than rectangular double-layer behavior. With increasing scan rate, the anodic and cathodic peaks shift apart because of polarization and finite ion-transport time. The individual potential windows in Fig. 5b–d differ, so their enclosed areas are used only to assess shape evolution, not to rank capacitance.

The b-values obtained from log(i) versus log(v) are 0.45 and 0.47 for the $CuCo_2O_4$ oxidation and reduction peaks, 0.643 and 0.531 for $CuNi_2O_4$, and 0.625 and 0.497 for $CoFe_2O_4$. Values below or close to 0.5 indicate strong diffusion control at the measured peaks, whereas values between 0.5 and 1 indicate mixed surface and diffusion behavior. These values are consistent with the battery-like redox plateaus in the GCD curves and do not support a purely pseudocapacitive assignment [27-31].

Current separation using $k_1v + k_2v^{1/2}$ shows that the fitted diffusion-controlled fraction of $CuCo_2O_4$ increases from 84% to 93% between 0.5 and 2.5 mV s^{-1}, whereas the corresponding fractions decrease from 80% to 63% for $CuNi_2O_4$ and from 82% to 68% for $CoFe_2O_4$. The $CuCo_2O_4$ trend should not be interpreted as faster diffusion at higher scan rates. It is an empirical consequence of the fitted current distribution within a narrow low-rate range and is accompanied by increasing peak separation. For the other two oxides, the increasing surface-controlled fraction indicates that the outer redox sites become relatively more accessible as the diffusion depth decreases. The comparison demonstrates that a single b-value or contribution percentage cannot fully describe a porous battery-type electrode [32, 33].

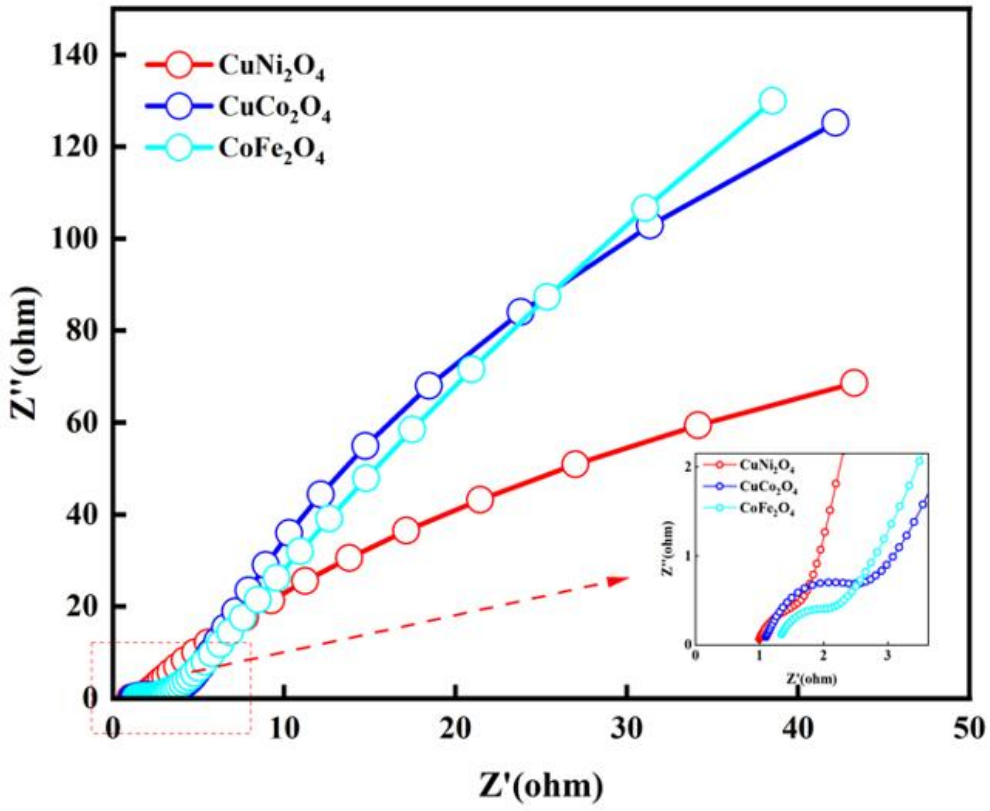


Fig. 4 Nyquist plots of $CoFe_2O_4$, $CuCo_2O_4$ and $CuNi_2O_4$ fiber electrodes in 1 mol L^{-1} KOH. Semicircle sizes and low-frequency slopes are compared qualitatively because an equivalent-circuit fit was not reported

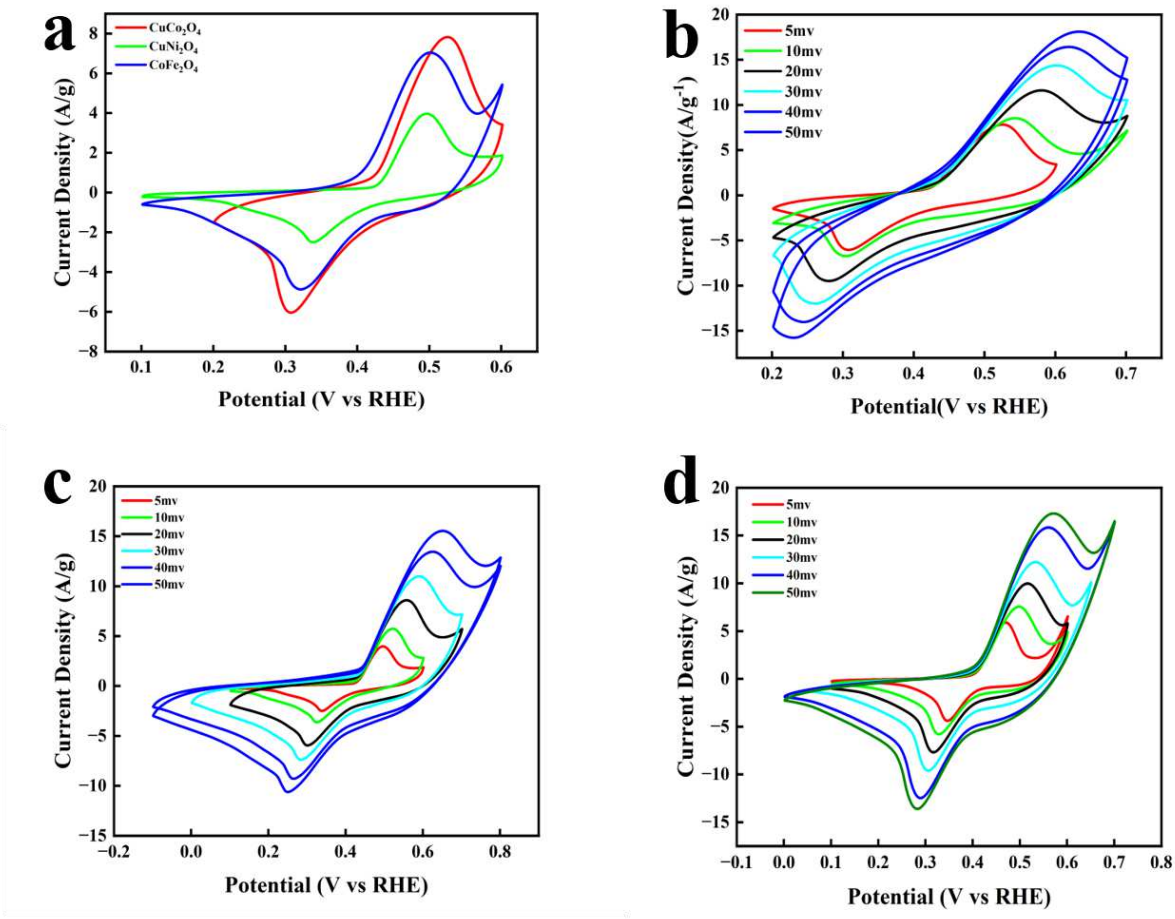


Fig. 5 CV curves of the three spinel fibers. (a) Matched-window comparison at 5 mV s^{-1} and CV curves of (b) $CuCo_2O_4$, (c) $CuNi_2O_4$ and (d) $CoFe_2O_4$ over their respective scan-rate ranges

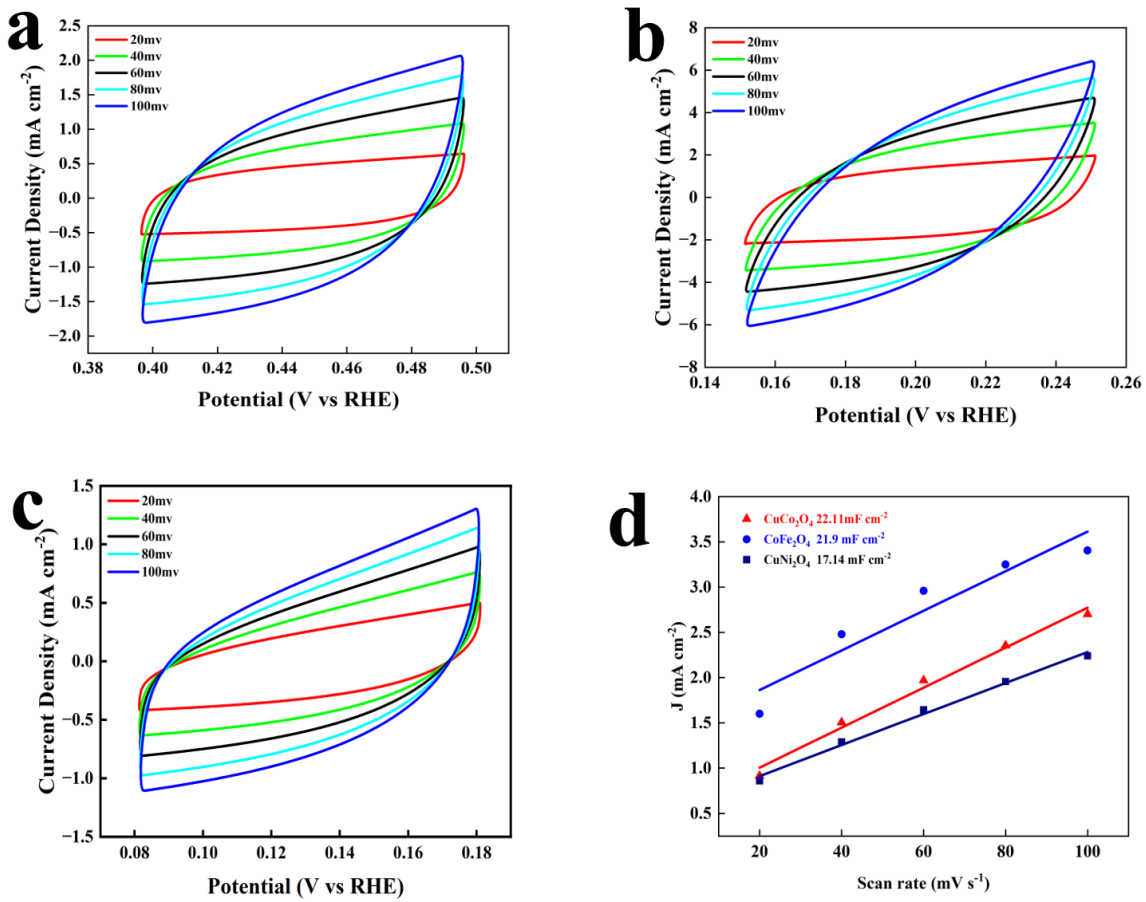


Fig. 6 CV curves used to estimate the non-Faradaic current response of (a) $CuCo_2O_4$, (b) $CuNi_2O_4$ and (c) $CoFe_2O_4$, and (d) the corresponding capacitive-current analysis

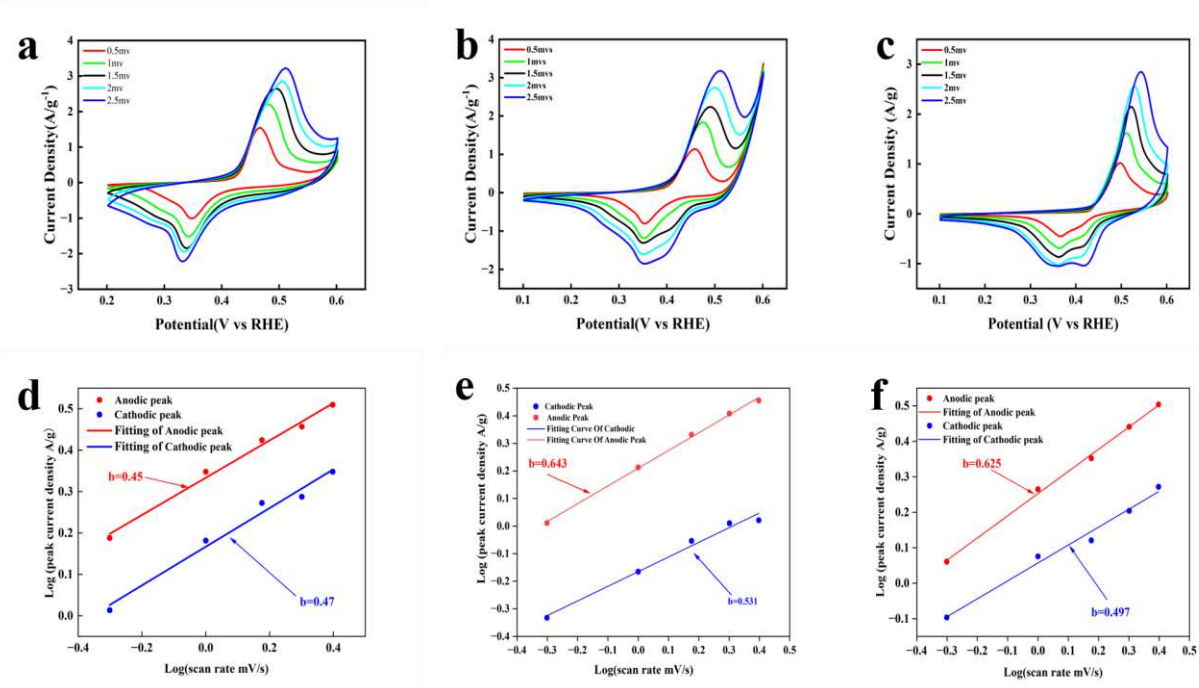


Fig. 7 Low-scan-rate CV curves of (a) $CuCo_2O_4$, (b) $CuNi_2O_4$ and (c) $CoFe_2O_4$, and log(i) versus log(v) plots for (d) $CuCo_2O_4$, (e) $CuNi_2O_4$ and (f) $CoFe_2O_4$

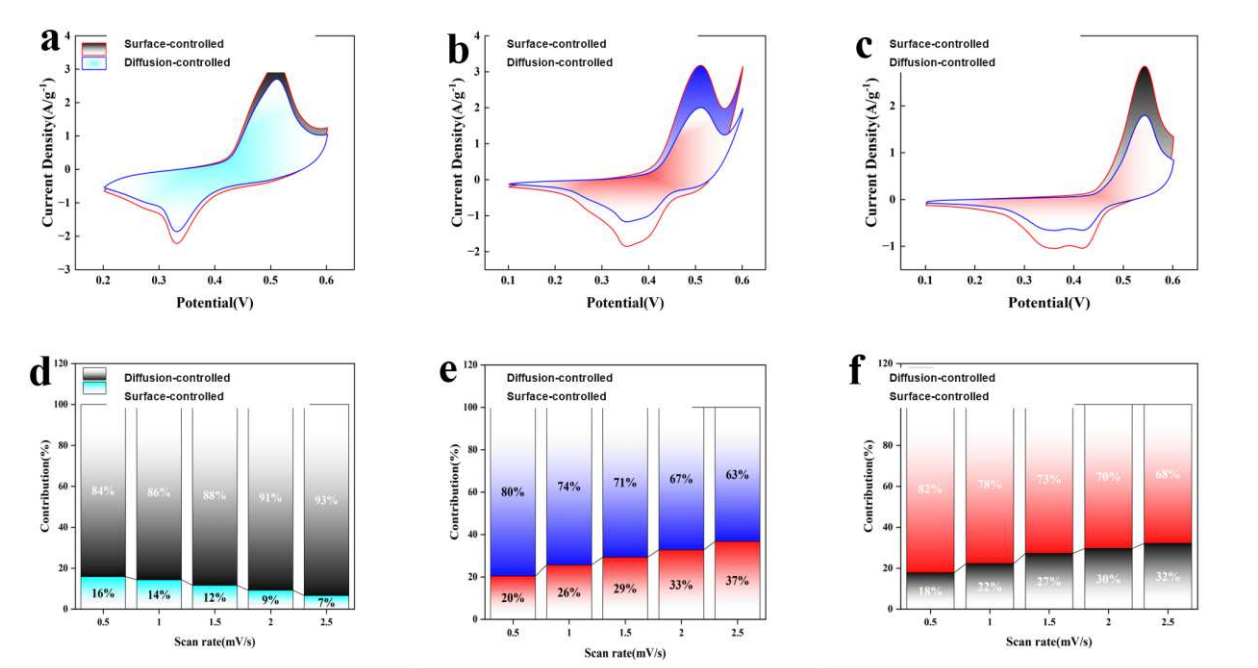


Fig. 8 Surface-controlled and diffusion-controlled current contributions of (a) $CuCo_2O_4$, (b) $CuNi_2O_4$ and (c) $CoFe_2O_4$ at 2.5 mV s^{-1}, and the evolution of the fitted contributions with scan rate for (d) $CuCo_2O_4$, (e) $CuNi_2O_4$ and (f) $CoFe_2O_4$

3.5 Galvanostatic charge storage and composition effects

The GCD curves in Fig. 9a–c are nonlinear and contain voltage plateaus, consistent with battery-type Faradaic storage rather than ideal capacitive behavior. At 1 A g^{-1}, $CuCo_2O_4$, $CoFe_2O_4$ and $CuNi_2O_4$ deliver 484, 406 and 220 F g^{-1}, respectively. The ordering agrees with the matched-window CV result in Fig. 5a and with the greater redox-current response of the Co-containing oxides. At 4 A g^{-1}, the approximate values are 200, 220 and 108 F g^{-1}, corresponding to relative retentions of about 41%, 54% and 49%. $CoFe_2O_4$ therefore provides the best rate retention even though $CuCo_2O_4$ provides the highest low-current capacitance.

This trade-off reflects the different rate-limiting steps. $CuCo_2O_4$ has a high accessible capacity at low current but loses a larger fraction when the discharge time is shortened, consistent with its strong diffusion-controlled character. $CoFe_2O_4$ begins with a lower capacity but retains comparatively more of it, indicating that a larger fraction of its active sites remains accessible at high current. $CuNi_2O_4$ combines the smallest charge-transfer semicircle with the lowest total capacitance and a shallower diffusion tail, showing that rapid interfacial charge transfer alone does not guarantee high active-site utilization. The composition-dependent balance among redox-site density, electronic transport and ion accessibility is therefore the key result [34, 35].

Table 3 Specific capacitance and rate-retention comparison obtained under the same three-electrode protocol

Electrode	Cs at 1 A g^{-1} (F g^{-1})	Approximate Cs at 4 A g^{-1} (F g^{-1})	Relative retention (%)	Observed kinetic limitation
$CuCo_2O_4$	484	200	≈41	High low-rate capacity; stronger diffusion limitation
$CoFe_2O_4$	406	220	≈54	Best relative rate retention among the three
$CuNi_2O_4$	220	108	≈49	Lowest charge-transfer resistance but limited utilization

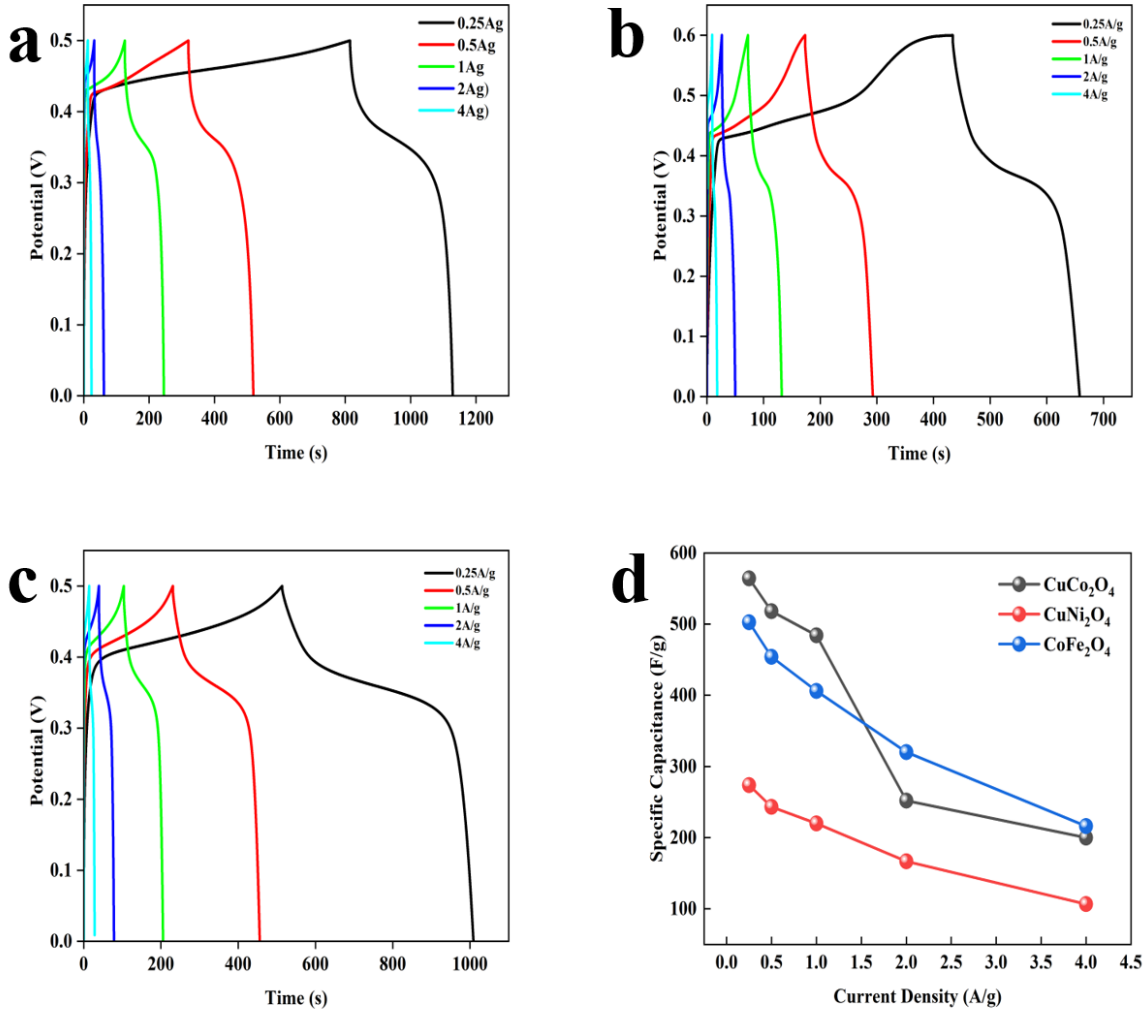


Fig. 9 GCD curves of (a) $CuCo_2O_4$, (b) $CoFe_2O_4$ and (c) $CuNi_2O_4$ at different current densities, and (d) the corresponding specific capacitances

3.6 Electrochemical performance of the asymmetric device

Fig. 10a shows that the $CuCo_2O_4$//activated-carbon device retained 99.93% of its initial capacitance after 5000 cycles, with a coulombic efficiency of 99.96%. These values are close to unity and are reported as measured under the tested coin-cell conditions. A post-cycling CV series, EIS spectrum and selected GCD profiles are shown in Fig. 10b–d. The CV curves remain non-rectangular and preserve their redox character, while the EIS response retains a small high-frequency feature and a sloping low-frequency region. The GCD profiles for cycles 4993–5000 are consistent with those recorded during early cycling, in agreement with the high measured retention.

The near-unity cycling metrics should be interpreted within the resolution and reproducibility of the experiment; they are not a claim of zero degradation. The device was used to verify that the $CuCo_2O_4$ fiber electrode can operate in an asymmetric configuration, not to optimize energy or power density through detailed mass balancing. Longer-term cycling, post-mortem phase analysis and electrolyte/electrode optimization remain necessary before practical claims can be made.

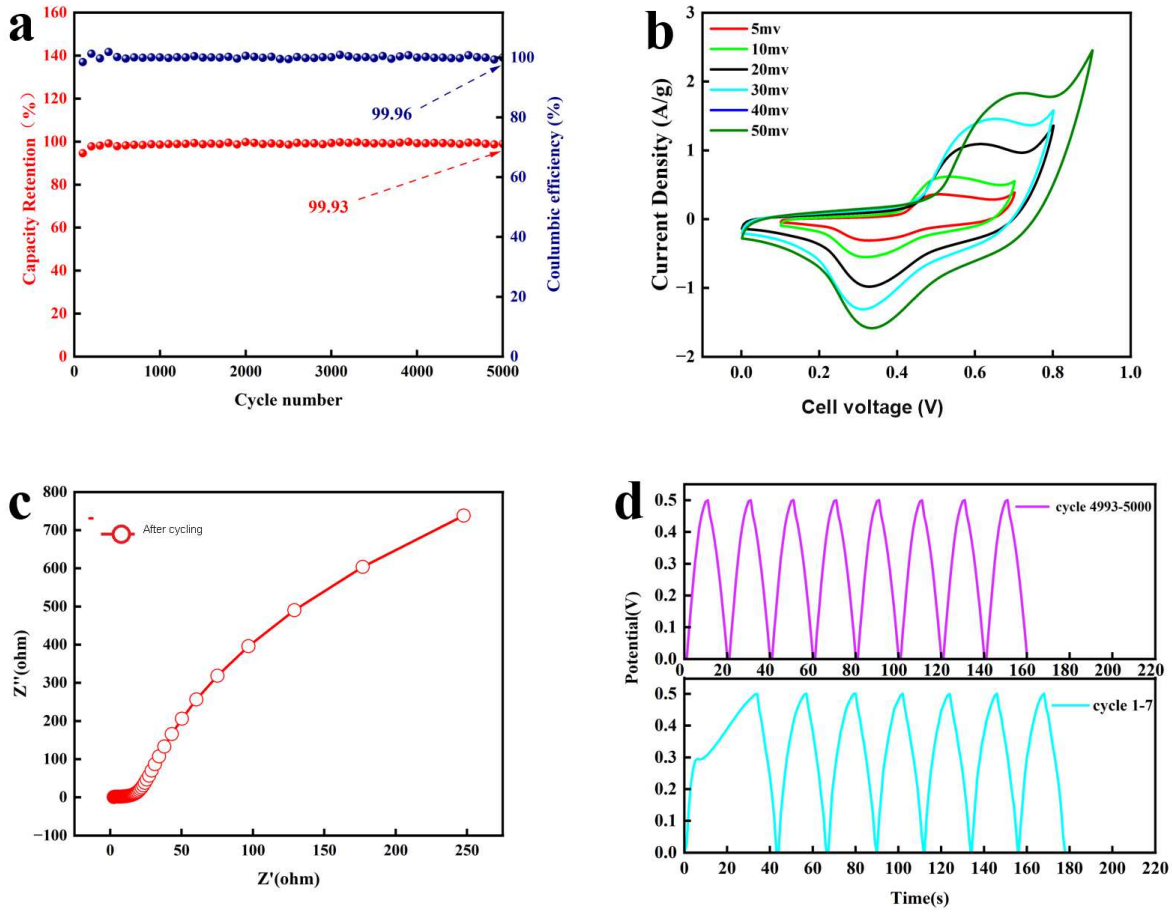


Fig. 10 Electrochemical performance of the $CuCo_2O_4$//activated-carbon device: (a) capacitance retention and coulombic efficiency over 5000 cycles; (b) post-cycling CV curves at different scan rates; (c) post-cycling Nyquist plot; and (d) GCD profiles at early and late cycle numbers

3.7 Scope and limitations

The comparative design reduces processing-related ambiguity, but several limitations remain. The XRD analysis identifies phase families from plotted patterns and does not provide refined lattice parameters, crystallite sizes or quantitative phase fractions. XPS binding energies constrain the possible valence states, but the absence of fitted component areas prevents quantitative Co^{2+}/Co^{3+} or Ni^{2+}/Ni^{3+} ratios. The electrochemical comparison uses geometric current density and a fixed active-material ratio; it does not isolate electronic conductivity from porosity or surface area. Finally, the device cycling result demonstrates stability under one coin-cell configuration and should not be generalized to all mass loadings or electrolytes. These constraints define the conclusions and indicate the experiments needed for further optimization.

4 Conclusion

Three compositionally distinct spinel oxide nanofibers were prepared under identical electrospinning and calcination conditions. XRD showed that $CoFe_2O_4$, $CuCo_2O_4$ and $CuNi_2O_4$ possess separate phase-specific reflection families, so a single common peak assignment is inappropriate. XPS identified multivalent Co, Cu and Ni centers together with Fe^{3+} and surface oxygen species, providing a chemically consistent basis for the Faradaic response. At 1 A g^{-1}, $CuCo_2O_4$ delivered the highest specific capacitance of 484 F g^{-1}, followed by $CoFe_2O_4$ at 406 F g^{-1} and $CuNi_2O_4$ at 220 F g^{-1}. $CoFe_2O_4$ showed the best relative rate retention, reaching approximately 54% at 4 A g^{-1}. The kinetic analysis demonstrates that charge storage is battery-like and that rapid interfacial charge transfer does not necessarily produce the highest accessible capacity. A $CuCo_2O_4$//activated-carbon device retained 99.93% of its initial capacitance with a coulombic efficiency of 99.96% after 5000 cycles. These results show that cation composition controls the coupled redox, transport and utilization behavior of electrospun spinel electrodes, providing a more reliable design principle than morphology or crystallinity alone.

Statements and Declarations

Funding

This work was supported by the Sichuan Province Science and Technology Program (Grant No. 2020JDRC0070).

Competing interests

The authors have no relevant financial or non-financial interests to disclose.

Ethics approval

This study did not involve human participants or animals.

Consent to participate and publication

Not applicable.

Data availability

The data supporting the findings of this study are presented in the article. Raw XRD, XPS, CV, GCD and EIS files are available from the corresponding author on reasonable request.

Author contributions

Pengyu Mao contributed to data collection and drafted the manuscript. Hengquan Liu conceived and supervised the study and contributed to manuscript editing. Yujie Liu and Mengyang Li contributed to data analysis and literature review. All authors read and approved the final manuscript.

References

[1] Mercante LA, Andre RS, Facure MHM, Correa DS, Mattoso LHC (2023) Recent progress in conductive electrospun materials for flexible electronics: Energy, sensing, and electromagnetic shielding applications. Chem Eng J 465:142847. https://doi.org/10.1016/j.cej.2023.142847

[2] Hu J, Zhang S, Tang B (2021) Rational design of nanomaterials for high energy density dielectric capacitors via electrospinning. Energy Storage Mater 37:530-555. https://doi.org/10.1016/j.ensm.2021.02.035

[3] Lin J, Karuppasamy K, Bose R, Vikraman D, Alameri S, Maiyalagan T, et al (2024) Research trends in electrospun conducting polymers derived CNFs and their composite as the potential electrodes for high-performance flexible supercapacitors. J Energy Storage 96:112605. https://doi.org/10.1016/j.est.2024.112605

[4] Du J, Jin B, Liao L, Shen X, Mei Z, Du Q, et al (2025) Facile synthesis of a high-entropy Oxide-Si nanocomposite via electrostatic spinning for lithium-ion battery electrodes. J Power Sources 659:238438. https://doi.org/10.1016/j.jpowsour.2025.238438

[5] Fleischmann S, Mitchell JB, Wang R, Zhan C, Jiang DE, Presser V, et al (2020) Pseudocapacitance: From Fundamental Understanding to High Power Energy Storage Materials. Chem Rev 120:6738-6782. https://doi.org/10.1021/acs.chemrev.0c00170

[6] Li X, Fu X, Zhang Y, Zhang Q, Wei Z, Wang K, et al (2025) Electrospun sodium titanate-MXene/carbon nanofibers as binder-free electrode for enhanced hybrid capacitive deionization. Chem Eng J 511:162040. https://doi.org/10.1016/j.cej.2025.162040

[7] Dubey R, Guruviah V (2019) Review of carbon-based electrode materials for supercapacitor energy storage. Ionics 25:1419-1445. https://doi.org/10.1007/s11581-019-02874-0

[8] Simon P, Gogotsi Y (2020) Perspectives for electrochemical capacitors and related devices. Nat Mater 19:1151-1163. https://doi.org/10.1038/s41563-020-0747-z

[9] Wang G, Zhang L, Zhang J (2012) A review of electrode materials for electrochemical supercapacitors. Chem Soc Rev 41:797-828. https://doi.org/10.1039/c1cs15060j

[10] Song JY, Kim DY, Yun HJ, Kim JH, Yi CC, Park SM (2022) Electroconductive, flexible, and printable graphene nanoplate-carbon nanotube-polydimethylsiloxane composite collectors for three-dimensional conformal electrospinning. Compos Sci Technol 227:109629. https://doi.org/10.1016/j.compscitech.2022.109629

[11] Cui S, Gao M, Li G, Gao X (2021) Insights into Li-Rich Mn-Based Cathode Materials with High Capacity: from Dimension to Lattice to Atom. Adv Energy Mater 12. https://doi.org/10.1002/aenm.202003885

[12] Liu Q, Wang T, Wang C, Wu D (2024) Coal tar pitch-derived porous carbon prepared in deep eutectic spinning solution via electrospinning for supercapacitor electrodes. Chem Eng J 481:148292. https://doi.org/10.1016/j.cej.2023.148292

[13] Dai J, Li J, Wang K, Li J, Tong X, Guo D, et al (2025) Electrospinning fabrication of ethanol lignin/polyacrylonitrile composite carbon fibers for supercapacitor applications. Int J Biol Macromol 322:146743. https://doi.org/10.1016/j.ijbiomac.2025.146743

[14] Kolathodi MS, Akbarinejad A, Tollemache C, Zhang P, Travas-Sejdic J (2022) Highly stretchable and flexible supercapacitors based on electrospun PEDOT:SSEBS electrodes. J Mater Chem A 10:21124-21134. https://doi.org/10.1039/d2ta04476e

[15] Khadka A, Pradhan S, Joshi B, Samuel E, Gao H, Aldalbahi A, et al (2024) ZnO-embedded activated carbon nanofibers derived from electrospun ZIF-7/metal salt/PAN fibers for flexible supercapacitors. J Alloys Compd 1002:175126. https://doi.org/10.1016/j.jallcom.2024.175126

[16] Manojkumar K, Muthuramalingam M, Sundamoorthy A, Srinivasa Babu PS, Vamsi R, Boominathan J, et al (2025) Revolutionizing energy storage: Self-charging supercapacitors toward self-powered micro and nano systems. Chem Eng J 524:168642. https://doi.org/10.1016/j.cej.2025.168642

[17] Ding W, Gao Y, Zhang Y, Zou Z, Jiang C (2022) MoSe2 nanosheets confined in N-doped carbon fibers as robust and capacitive anode of high performance Na-ion capacitors. J Energy Storage 52:104669. https://doi.org/10.1016/j.est.2022.104669

[18] Swain S, Sundaray B (2026) High-performance carbon nanofiber/vanadium pentoxide hybrid membranes for next-generation supercapacitors. J Energy Storage 163:122198. https://doi.org/10.1016/j.est.2026.122198

[19] Swain S, Sundaray B (2025) Electrospun free-standing MnO2/carbon nanofiber composite as battery-type electrode for advanced supercapacitor applications. J Energy Storage 134:118061. https://doi.org/10.1016/j.est.2025.118061

[20] Salih AJS, Huseyin A (2025) Nitrogen-doped MXene for supercapacitor: A review. J Energy Storage 131:117521. https://doi.org/10.1016/j.est.2025.117521

[21] Zheng Y, Man Z, Zhang Y, Wu G, Lu W, Chen W (2023) High-Performance Stretchable Supercapacitors Based on Centrifugal Electrospinning-Directed Hetero-structured Graphene–Polyaniline Hierarchical Fabric. Adv Fiber Mater 5:1759-1772. https://doi.org/10.1007/s42765-023-00304-5

[22] Mohamed N, Aboelazm E, Soaid NI, Roslan SAH, Jose R, Saheed MSM (2025) Sustainable electrospun carbon fibre electrodes from dealkaline lignin: Towards enhanced energy storage in supercapacitors. J Energy Storage 140:118972. https://doi.org/10.1016/j.est.2025.118972

[23] Biesinger MC, Payne BP, Grosvenor AP, Lau LWM, Gerson AR, Smart RSC (2011) Resolving surface chemical states in XPS analysis of first row transition metals, oxides and hydroxides: Cr, Mn, Fe, Co and Ni. Appl Surf Sci 257:2717-2730. https://doi.org/10.1016/j.apsusc.2010.10.051

[24] Biesinger MC, Lau LWM, Gerson AR, Smart RSC (2010) Resolving surface chemical states in XPS analysis of first row transition metals, oxides and hydroxides: Sc, Ti, V, Cu and Zn. Appl Surf Sci 257:887-898. https://doi.org/10.1016/j.apsusc.2010.07.086

[25] Gaberšček M (2022) Impedance spectroscopy of battery cells: Theory versus experiment. Curr Opin Electrochem 32:100917. https://doi.org/10.1016/j.coelec.2021.100917

[26] Orazem ME, Itagaki M (2025) Electrochemical Impedance Spectroscopy. Electrochem Soc Interface 34:59-59. https://doi.org/10.1149/2.f08253if

[27] Samuel E, Khadka A, Joshi B, Gao H, More S, Aldalbahi A, et al (2024) Electrospun carbon/iron–vanadium oxide nanofibers for high energy density supercapacitors. Chem Eng J 499:156413. https://doi.org/10.1016/j.cej.2024.156413

[28] Zhou S, Jang H, Qin Q, Hou L, Kim MG, Liu S, et al (2022) Boosting Hydrogen Evolution Reaction by Phase Engineering and Phosphorus Doping on Ru/P-TiO 2. Angew Chem Int Ed 61. https://doi.org/10.1002/anie.202212196

[29] Guan J, Chen W, Fang Y, Wang L, Fu Y, Guo B, et al (2022) Electrospinning derivative fabrication of sandwich-structured CNF/Co3S4/MoS2 as self-supported electrodes to accelerate electron transport in HER. Int J Hydrogen Energy 47:14930-14941. https://doi.org/10.1016/j.ijhydene.2022.03.013

[30] Lu F, Ji Y, Shi D, Yao J, Pei L (2023) Electrochemically activated 3D Mn doped NiCo hydroxide electrode materials toward high-performance supercapacitors. J Colloid Interface Sci 641:510-520. https://doi.org/10.1016/j.jcis.2023.03.081

[31] Wang W, Zhou Y, Sun P, Liu L, Guo C, Wang X, et al (2024) One-step synthesis of double-walled NiCo2O4 hollow nanotubes using hollow fiber templates created by airflow-coaxial electrospinning. Vacuum 228:113526. https://doi.org/10.1016/j.vacuum.2024.113526

[32] Gan Z, Ren X, Sun Y, Sun M, Yan Y, Cao B, et al (2023) Highly porous nanocomposites of Mn doped cobalt-based hydroxide/sulfide as high-performance electrode materials for hybrid supercapacitors. J Energy Storage 69:107934. https://doi.org/10.1016/j.est.2023.107934

[33] Sengodan P, Yang X, Tang Y, Dhanushkodi S, Zhang R, Li B, et al (2025) Mn-substituted spinel zinc cobaltite nanoplates as electrode materials for solid-state asymmetric supercapacitors. J Power Sources 660:238436. https://doi.org/10.1016/j.jpowsour.2025.238436

[34] Ding C, Yuan M, Cao X, Tang X, Zhao Y, Hao W, et al (2023) Electrochemical performance of asymmetric supercapacitors based on NiCo(OH)4/Cu2(OH)3NO3 electrode. Mater Today Chem 34:101775. https://doi.org/10.1016/j.mtchem.2023.101775

[35] Zhong X, Liu X, Li Z, Wang C, Dmytro S (2023) Electrodeposited ultra-thin FeCo2O4 nanosheets on nickel foam as binder-free electrodes for high-performance supercapacitors. J Energy Storage 73:109257. https://doi.org/10.1016/j.est.2023.109257

[36] Amirthavalli R, Begum AN, Parthibavarman M, Tamilchezhiyan M (2025) Enhancing the electrochemical properties of Sr-doped spinel copper cobaltite CuCo2O4 for supercapacitor application. Ionics 31:5217-5236. https://doi.org/10.1007/s11581-025-06241-0

[37] Rajashekar KR, Sagar MD, Mahanthesha KR, Karthik G, Urs GT, Gowtham GK (2026) Ternary spinel $CuNiMnO_4$/MWCNT: a high-capacitance electrode for supercapacitor applications. Ionics. https://doi.org/10.1007/s11581-026-07633-6

[38] K. AD, S. K, K. K, M. M (2025) Tailoring the structural and electrochemical properties of $CuNi_2O_4$ spinel for high-performance hybrid supercapacitor electrodes. Ionics 31:11095-11114. https://doi.org/10.1007/s11581-025-06638-x